ADVANCED FUNCTIONAL MATERIALS
www.afm-journal.de

Optimizing (1-x) $BiFeO_3$-x$CaTiO_3$ Perovskites: A Pathway to Efficient Flexible Energy Storage

*Febin Paul, Shahina Shareef, Eric Kumi Barimah, Mustehsan Beg, Keng Goh, Gin Jose, Zhilun Lu, and Libu Manjakkal**

New advanced functional material manufacturing and electrode design are the keys to developing the next generation of smart energy storage devices. This study explores the electrochemical performances of (1-x) $BiFeO_3$-x$CaTiO_3$ ($x = 0.4, 0.5, 0.6$) (BFO-CTO) perovskite for flexible electrochemical capacitors (ECs). BFO-CTO are synthesized via solid-state reaction, ensuring phase purity, while electrodes are printed on a flexible graphene sheet. X-ray photoelectron spectroscopy (XPS) confirmed the mixture of metallic bismuth ($Bi^{(0)}$) and Bi_2O_3 (Bi^{3+}), enhancing charge through redox activity and conductivity. The 60BFO-40CTO composition exhibited a crystalline perovskite structure with high conductivity (14.03 kS.m^{-1}) and hydrophilic properties (contact angle 40.3°). This resulted in a high electrochemically active surface area of 1.059 x10^{-3} cm^2 and a specific capacitance of 2.79 mF.cm^{-2} in the symmetric EC. The asymmetric BF6CT4-G-EC, configuration achieved approximately an 80% increase in capacitance compared to the symmetric counterpart. It retained ≈90% of its initial capacitance after 6000 cycles, and maintained ≈72% capacity after 3000 cycles under 40° bending. These results highlight the potential of BFO-CTO perovskites as high-performance electrode materials for flexible energy storage applications.

1. Introduction

Rapid advancements in modern digital technologies have led to a growing demand for smart, flexible electronic devices in recent decades. To power these devices, there is a persistent need to develop flexible energy storage devices that can withstand deformation while maintaining their electrochemical and electrical functions.[1] The increase in demand for energy storage devices has raised concerns about the performance, cost, and availability of raw materials.[2] In this context, the high electrical and ionic conductivity of materials with perovskite structure makes them excellent for energy storage while being low-cost and widely available.[3] ABX_3 is considered the general formula for perovskite materials, where A and B are two cations of significantly different sizes, and X is an anion that bonds to both A and B. Large ions such as halides, nitrides, sulfides, and oxygen are the most commonly considered for the X site.[4] The most widely considered A-site cations in perovskites include alkaline earth metals like Ca^{2+}, Sr^{2+}, and Ba^{2+}; alkali metals such as Cs^+, Rb^+, and K^+; and rare earth elements like La^{3+} and Nd^{3+}. Transition metals, including Ti^{4+}, Zr^{4+}, Nb^{5+}, and Pb^{2+} are frequently used as B-site cations. Perovskite-based materials are attractive for electrolytic and electrochemical applications due to their key physical properties, including dielectric properties, ferroelectricity, ionic conduction, superconductivity, and insulator–to-metal transition.[3d,5] The Supporting Information provided in Tables S1 and S2 (Supporting Information) summarizes the performance of perovskite material for electrochemical and electrolytic energy storage.

As an electrochemical energy storage material, the perovskite structure can host various metal ions and anions, exhibiting excellent bulk intercalation/deintercalation. This allows them to store a maximum amount of charge by utilizing the electrochemically active surface area (ECSA).[3d] In electrochemical capacitor (EC) applications, the fast kinetics that reduce phase transformation during charging and discharging enhance the power density for perovskites as discussed by Goel et al. and Mohan et al.[3a,b] Perovskite-structured materials inherently contain oxygen vacancies, which can lead to a high specific capacitance as discussed by Ahangari et al. for $SrFe_xCo_{1-x}O_{3-\delta}$ perovskite oxides as a supercapacitor electrode material.[6] In addition, perovskite functions as an electrolytic capacitor (ELCs) for energy storage due to its high dielectric constant, charge carrier mobility, tunability, low cost, scalability, and chemical stability. These properties make them promising candidates for improving the performance and efficiency of energy storage devices.[7] Among various perovskite

F. Paul, S. Shareef, M. Beg, K. Goh, Z. Lu, L. Manjakkal
School of Computing and Engineering & the Built Environment
Edinburgh Napier University
Merchiston Campus, Edinburgh EH10 5DT, UK
E-mail: L.Manjakkal@napier.ac.uk
E. K. Barimah, G. Jose, Z. Lu
School of Chemical and Process Engineering
University of Leeds
Leeds LS2 9JT, UK

The ORCID identification number(s) for the author(s) of this article can be found under https://doi.org/10.1002/adfm.202507692

DOI: 10.1002/adfm.202507692

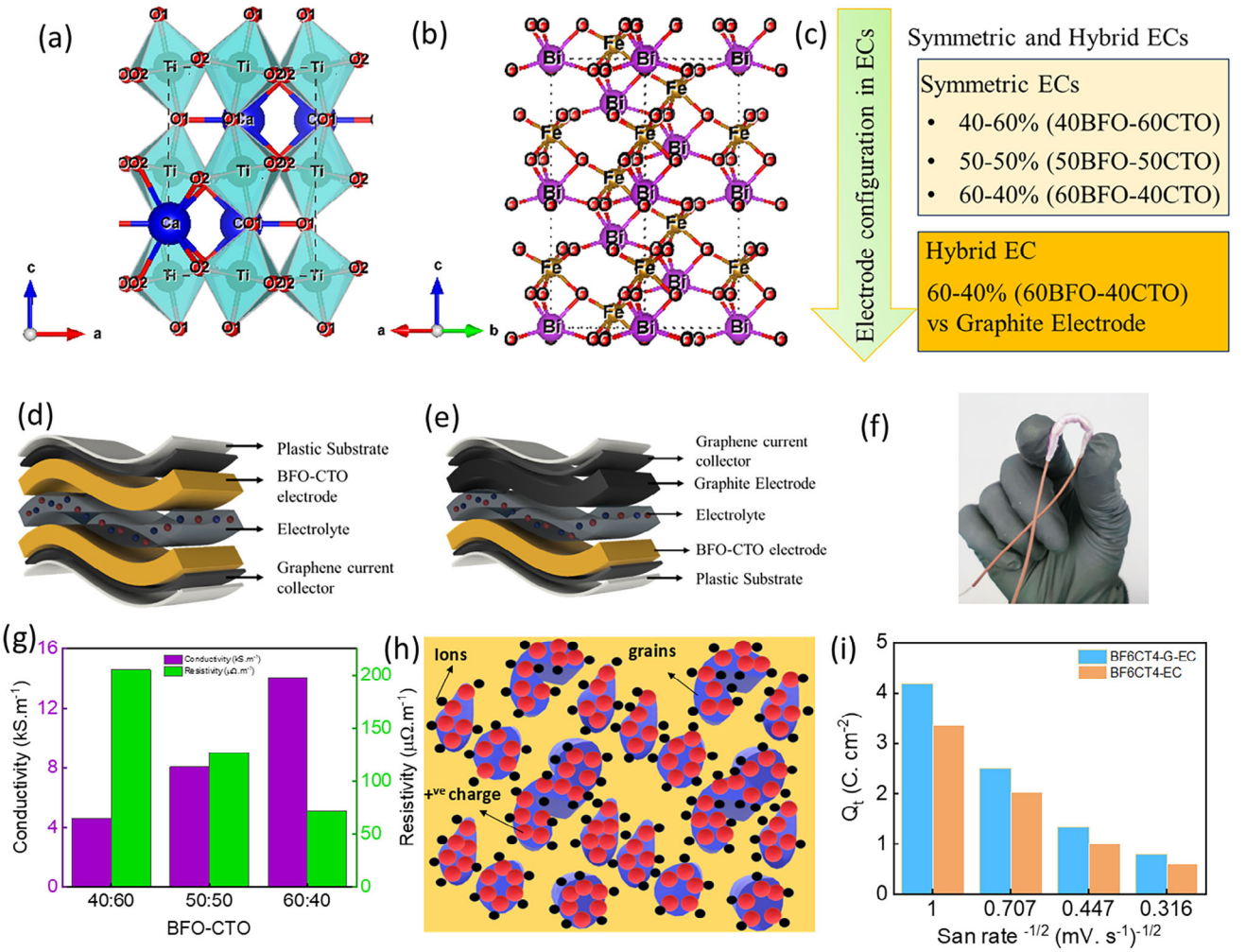

Figure 1. a) Crystalline structure of $CaTiO_3$ (CTO). b) Crystalline structure of $BiFeO_3$ (BFO). c) Electrode configuration used in the design of symmetric and asymmetric ECs. Schematic representation of d) Symmetric EC-based BFO-CTO electrode, e) Asymmetric EC-based BFO-CTO Vs graphite electrode and f) Image of developed flexible EC, g) Variation of electrical conductivity and resistivity of the printed 40BFO-60CTO, 50BFO-50CTO, 60BFO-40CTO films, h) Ions distribution around multiple grains of the composite electrode during the interaction with electrolyte and i) Charge contribution of BF6CT4-EC (symmetric) and BF6CT4-G-EC (asymmetric).

materials, $BiFeO_3$ (BFO) and $CaTiO_3$ (CTO) are recognized as excellent materials for energy storage devices. Recently, Gomasu et al., reported the high energy density performances of BFO-CTO as an ELC material for high temperature applications.[7] Here, the CTO is acknowledged as the prototypical perovskite, featuring a specific arrangement of atoms in a crystalline lattice, as shown in **Figure** 1a. Six oxygen atoms (O^{2-}) surround the central calcium ion in an octahedral arrangement. The O^{2-} ions form the corners of an octahedron, with the calcium ion positioned at the center of this octahedron. Titanium ions (Ti^{4+}) occupy the corners of the unit cell, located at the vertices of the cube formed by the oxygen octahedra. This arrangement repeats throughout the crystal lattice to form the calcium titanite structure.[8]

Moreover, CTO crystals typically exhibit well-defined facets and geometric shapes due to the regular arrangement of atoms in the crystal lattice. They can appear as cubic, octahedral, or other polyhedral shapes. The growth method can also influence the size and morphology of CTO crystals. Crystals can be synthesized using sol-gel methods, hydrothermal methods, and solid-state reactions.[9] Due to its high pore volume, hierarchical pore structure, and exceptional conductivity, the optimized activated carbon/CTO demonstrated good capacitance at low current density in a two-electrode system with 6 M KOH as the electrolyte. BFO is a conventional ABO_3-structured perovskite material, as represented in Figure 1b, with A and B sites occupied by Bi and Fe, respectively. In the case of bismuth ferrite, the central cation is a bismuth ion (Bi^{3+}). Six O^{2-} ions surround the central Bi^{3+}, forming an oxygen octahedron similar to the standard perovskite structure. Iron ions (Fe^{3+}) are located at the corners of the unit cell, and these Fe^{3+} ions are also connected to O^{2-} ions to form an octahedral arrangement that shares edges with the central oxygen octahedron.[10] Recently, a high-performance EC was reported by Moitra et al., using BFO nanowire-RGO nanocomposite with excellent cyclic stability.[10a] Induced anion defect sites improve the electrochemical performance of BFO due to their crystal structure. Jo and team found that, the $BiFeO_{3-X}$ electrode

exhibits a capacitance of 923.8 mF.cm^{-2}, while $BiFeO_3$ shows 300.9 mF.cm^{-2}, demonstrating high electrochemical stability.[11] BFO-based ceramics are also considered promising contenders for high-energy-density capacitors, thanks to BFO's significant spontaneous polarization and elevated Curie temperature (T_c).[12]

In this study, we prepared and evaluated a perovskite material (1-x) $BiFeO_3$-x$CaTiO_3$ (x = 0.4, 0.5, 0.6) for energy storage applications as a novel flexible EC. $BiFeO_3$-$CaTiO_3$ with three ratios of 40-60% (40BFO-60CTO), 50-50% (50BFO-50CTO), and 60-40% (60BFO-40CTO) was used as the active material for the electrode's fabrication, given in Table S3. The electrodes used for the development of symmetric and asymmetric ECs are summarized in Figure 1c. Based on these electrodes, three individual symmetric ECs were developed, as schematically shown in Figure 1d and evaluated. The 60BFO-40CTO-based electrode exhibited a specific capacitance of 2.79 mF.cm^{-2}, and the image of the device is shown in Figure 1f, which is higher than that of the 40BFO-60CTO and 50BFO-50CTO electrode-based devices. The BFO-CTO electrode with the best performance ratio and a graphite electrode were used to develop a flexible asymmetric EC, as schematically shown in Figure 1e. In symmetric and asymmetric EC fabrication, cellulose cloth and 6 M KOH were used as the separator and electrolyte, respectively. Transition metals in perovskite materials, like Fe in $BaFeO_3$, can exist in different oxidation states, such as Fe^{3+} and Fe^{2+}.[13] These changes in oxidation states affect the material's electronic properties and how it interacts with electrolyte ions like hydroxide (OH^-) from KOH. The ability of these metals to switch between oxidation states can change their surface charge and reactivity, influencing how ions are adsorbed or desorbed.[14] When transition metals undergo redox reactions, the surface charge of the material can change, which may attract or repel KOH ions and affect how much is adsorbed. Additionally, these redox processes can shift the electrochemical potential of the surface, making it easier to adsorb OH^- or K^+ ions from KOH. In alkaline environments (like those with KOH), metal oxides can help adsorb OH^- ions, especially when the metal is undergoing redox reactions. This can improve the material's electronic structure, catalytic properties, or ionic conductivity.[3d,15] The combination of BFO, where Fe can exist in multiple oxidation states, and CTO, which has Ti in a stable state, could create a synergistic effect on KOH ion adsorption. The Fe^{3+}/Fe^{2+} redox couple in BFO may help alter the material's charge, encouraging more adsorption of KOH ions. Meanwhile, CTO could affect the stability and structure of the composite, influencing how well it adsorbs ions.[3d,16] Overall, the redox behavior of transition metals in BFO-CTO materials is important for how KOH electrolyte ions are adsorbed. This interaction impacts the material's electrochemical properties and is crucial for optimising its performance in electrochemical devices. During this study, we observed high conductivity (Figure 1g), excellent wettability (**Figure 2i–l**), and many structurally oriented grains and particles of varying sizes with multiple pores, as shown in Figure 1h, leading to enhanced ECSA during the electrochemical reactions in BF6CT4-EC. In addition, we observed that changing the electrode configuration enhances the ECSA. For the asymmetric EC, the ECSA is 1.059×10^{-3} cm^2, which is 1.73 times higher than that of the symmetric EC with the electrode (60BFO-40CTO). As a result, the asymmetric EC device can store more charge than the symmetric EC, as shown in Figure 1i. The asymmetric EC exhibited a specific capacitance of 3.5 mF.cm^{-2} at one mV.s^{-1}. The static bending analysis at different angles of the BFO-CTO confirmed the suitability of the developed EC.

2. Results and Discussion

2.1. Structural and Morphological Characterization

The full-pattern X-ray Diffractometer (XRD) Rietveld refinement results of the (1-x)BFO-xCTO (x = 0.4, 0.5, 0.6) powders obtained at room temperature are presented in Figure 2a–c and Table S4 (Supporting Information). The lattice parameters for each composition were determined by fitting with a fixed background and peak type, which allowed for calculating the cell volume and refinement of the parameters. All the diffraction peaks observed in the XRD pattern can be accurately attributed to a singular orthorhombic perovskite structure with a *Pbmn* space group. To our knowledge, only the crystal structure information for x = 0.6 has been reported previously, with a cell volume of 235.29 Å^3,[17] and our data is consistent with this reported value. As shown in Table S4 (Supporting Information), an increase in CTO content leads to a reduction in all lattice parameters and a decrease in the unit cell volumes. This indicates that forming a solid solution between BFO and CTO has been successfully achieved in these compositions. This is attributed to the fact that CTO, with a cell volume of 223.55 Å^3, has a smaller cell volume compared to BFO (373.67 Å^3).[18] The prepared crystalline powders were used for the fabrication of printed active electrodes. The surface morphology of these printed active electrodes plays a significant role in enhancing the interaction between the electrolyte and electrode in ECs.

The structural evolution of (1-x)BFO-xCTO composites (﹨(x = 0.4, 0.5, 0.6﹨)) was systematically investigated via XRD coupled with Rietveld refinement (Figure 2a–c). All compositions exhibited a single-phase orthorhombic perovskite structure, crystallizing in the *Pbmm* space group, which is consistent with the distorted perovskite framework commonly observed in mixed A/B-site substituted systems. The refinement process employed fixed background parameters and pseudo-Voigt peak profiles to optimize lattice constants, atomic positions, and thermal displacement parameters. Notably, the cell volumes derived from these refinements (Table S4, Supporting Information) decreased progressively with increasing CTO content—from 235.29 Å^3 for x = 0.6 to smaller values for x = 0.5 and x = 0.4—aligning with Vegard's law for solid solutions. This contraction arises from the substitution of larger Ba^{2+} (1.61 Å) and Fe^{3+} (0.645 Å) ions in BFO with smaller Ca^{2+} (1.34 Å) and Ti^{4+} (0.605 Å) ions in CTO, which reduces interatomic distances and compresses the unit cell. The successful formation of a homogeneous solid solution is further evidenced by the absence of secondary phases in the XRD patterns, confirming complete miscibility between BFO and CTO within the studied compositional range. While prior literature only reported structural data for x = 0.6 (cell volume = 235.29 Å^3),[17] this work extends the understanding to x = 0.4 and x = 0.5, revealing a linear correlation between CTO content and lattice contraction. This trend highlights the role of ionic size mismatch in tailoring structural properties, which is critical for optimizing functional behaviors such as dielectric response or ion

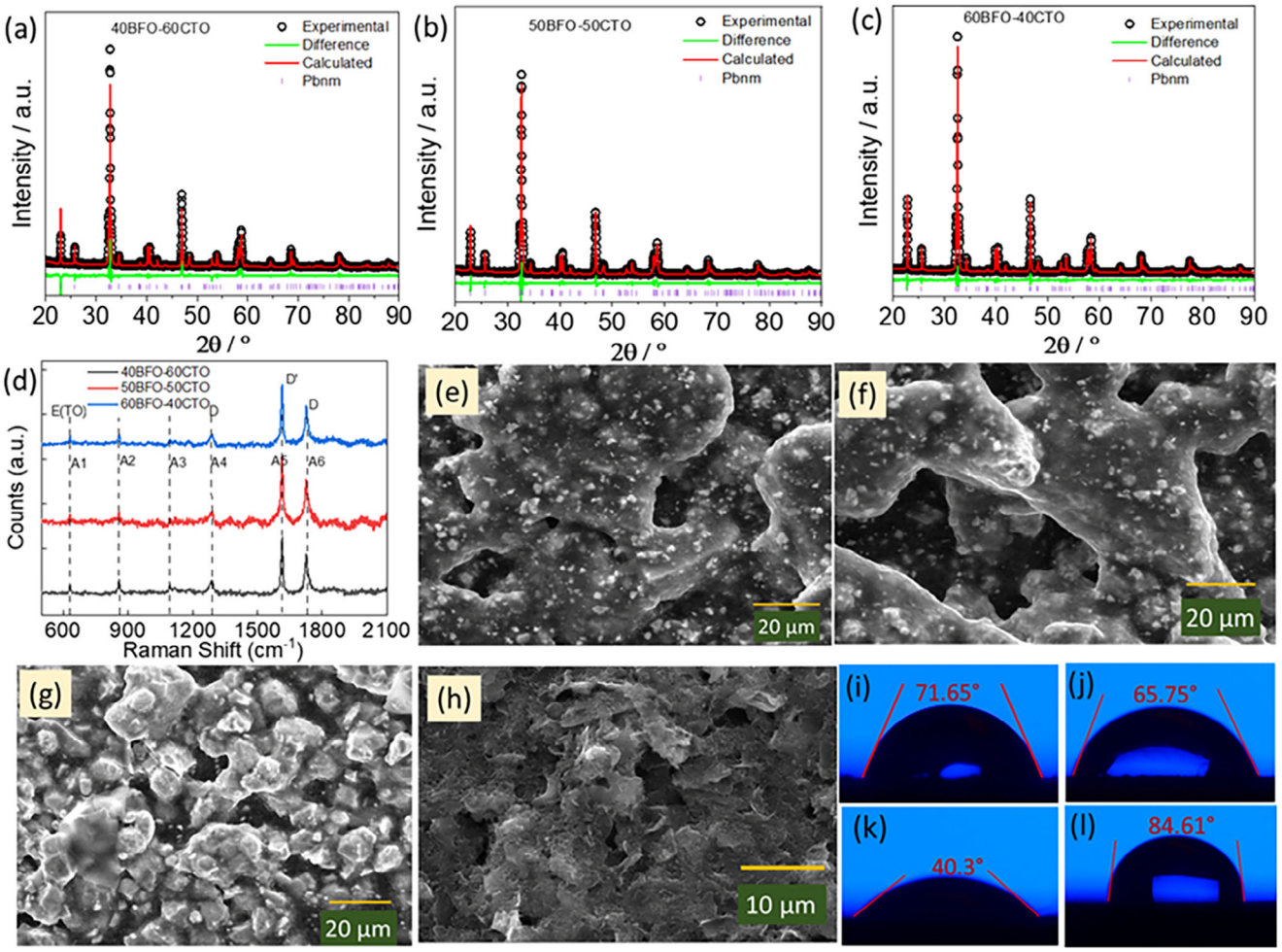

Figure 2. Structural and morphological properties of the electrode materials. a–c) XRD pattern and corresponding Rietveld refinement results for 40BFO-60CTO, 50BFO-50CTO, 60BFO-40CTO ceramics at room temperature. d) Raman spectra of the 40BFO-60CTO, 50BFO-50CTO, 60BFO-40CTO composite electrode. e–h) SEM images of 40BFO-60CTO, 50BFO-50CTO, 60BFO-40CTO, and graphite film respectively i–l) contact angle measurement of 40BFO-60CTO, 50BFO-50CTO, 60BFO-40CTO, and graphite film respectively.

transport. The refined powders were subsequently utilized to fabricate printed active electrodes for ECs. The reduced cell volume at higher CTO content $x = 0.6$ may enhance electrode-electrolyte interactions by increasing surface area or modifying pore structure, though further morphological analysis (e.g., SEM/TEM) is required to validate this hypothesis. Surface morphology, influenced by crystallite size and phase homogeneity, is expected to play a pivotal role in charge storage mechanisms, as smaller grain boundaries and defect-free interfaces typically improve ionic accessibility and charge transfer kinetics. These findings underscore the importance of compositional tuning in perovskite oxides for energy storage applications.

The Raman spectroscopy analysis of BFO-CTO heterostructures, conducted using a Renishaw Raman spectrometer with 488 nm laser excitation, provides critical insights into the structural and compositional characteristics of the composite electrode material. The composite electrodes incorporate ethyl cellulose as a binder and conductive carbon black as a filler, both of which influence the spectral features. In Figure 2d the Raman spectra shows six distinct vibration modes were observed within the 500–1800 cm^{-1} range, each corresponding to specific chemical bonds and molecular interactions. The A1 peak at 632 cm^{-1} is attributed to C–OH bending or stretching vibrations, likely arising from hydroxyl groups in the binder or adsorbed moisture. At 860 cm^{-1} (A2), HCC (alkyne) and HCO (carbonyl) bending modes suggest the presence of sp^2-hybridized carbon defects or functional groups associated with the carbon black filler. The A3 peak at 1095 cm^{-1} corresponds to C–C and C–O stretching motions, indicative of disordered carbon structures or residual polymer components. The A4 peak (1287 cm^{-1}) aligns with the disorder-induced D-band of graphitic carbon, reflecting structural imperfections in the conductive filler. The prominent A5 peak at 1615 cm^{-1} represents the G-band of ordered sp^2-hybridized carbon, underscoring the graphitic nature of the carbon black, which is critical for electrical conductivity. Finally, the A6 peak at 1727 cm^{-1} is assigned to C=O stretching vibrations, likely originating from oxidized carbon species or residual organic components, which may impact electrochemical stability. Notably, lower-frequency modes (<500 cm^{-1}), typically associated with Fe–O and Ti–O lattice vibrations in

pristine BFO and CTO, were absent in the composite. This absence may result from surface localization effects, where the binder and carbon filler dominate the near-surface region, masking deeper structural vibrations. Additionally, phonon damping by the conductive carbon black or interfacial strain-induced crystallographic disorder between BFO and CTO phases could suppress these modes. Comparative analysis with literature highlights consistency in assignments: identification of organic residues (C═O/C–O bonds),[19] while corroborates the role of disorder-induced D/G bands in carbonaceous materials.[20] The missing low-frequency modes, for other BFO-CTO systems, emphasize the unique interfacial dynamics of this composite.[21] The dominance of carbon-related peaks underscores the critical role of conductive fillers in enhancing electronic pathways but also raises considerations about interfacial reactivity, such as oxidation at C═O sites. The suppressed perovskite vibrations suggest strong interfacial coupling, which may influence ferroelectric or multiferroic properties.

A scanning electron microscope (SEM) was used to examine the surface morphology and microstructure of the BFO-CTO samples. Figure 2e–g shows that the electrode surfaces exhibit well-developed porous structures with large particles, particularly in the 50BFO-50CTO and 40BFO-60CTO samples. In contrast, the 60BFO-40CTO sample shows smaller particles with multiple tiny pores. This distribution of pores enhances charge storage in the active material of the 60BFO-40CTO electrode compared to the other two electrodes. Additionally, the surface morphology of the graphite electrode, which serves as the second terminal of the developed asymmetricEC, is shown in Figure 2h. The graphite-printed electrode displays a porous, flake-like structure. Elemental analysis was conducted using energy dispersive X-ray analysis (EDAX), with results in the Figure S2a–d (Supporting Information). These porous surfaces facilitate improved interaction with electrolytes, which was confirmed through the contact angle measurements. The contact angle measurement indicates that the BFO-CTO and graphite electrodes are hydrophilic, as shown in Figure 2i–l. Among the three BFO-CTO electrodes, the 60BFO-40CTO electrode exhibits the lowest phase angle, ≈40.3°. This suggests that the wettability is correlated with the porosity of the electrode, as the 60BFO-40CTO is more porous, resulting in better wettability, as shown in Figure 2g. The contact angles were measured immediately after the electrolyte was dropped on the surface, and we observed that the contact angle further decreased within 10 min, as shown in Figure S3a–h (Supporting Information). It was noted that the high porosity and wettability of graphite lead to rapid absorption of the electrolyte, with the contact angle decreasing from 84.61° initially and almost zero after 10 min, as shown in Figure 2l and Figure S3h (Supporting Information). This demonstrates the excellent performance of the graphite electrode, which allows ions to penetrate its core structure. In addition to crystallinity, porosity, and surface morphology variation, the changes in the ratio of BFO and CTO also lead to the improvement of the film's ionic and electronic conductivity. The variation in electrical conductivity is shown in Figure 1g, where the 60BFO-40CTO film exhibits a conductivity of 14.03 $kS.m^{-1}$, nearly three orders of magnitude higher than that of 40BFO-60CTO.

The X-ray Photoelectron Spectroscopy (XPS) survey and high-resolution spectra analysis of $BaFeO_3$-$CaTiO_3$ (BFO-CTO) composites with varying stoichiometries (60BFO-40CTO, 50BFO-50CTO, and 40BFO-60CTO) provide critical insights into their elemental composition, surface chemistry, and structural integrity. The survey spectra **Figure 3**a, confirm the presence of key constituent elements, including Fe (from BFO), Ca and Ti (from CTO), and O, consistent with the perovskite-based structure of the composites. Unexpectedly, Bi 4f signals were detected, which may arise from cross-contamination during synthesis or handling, or potentially from overlapping spectral features requiring further investigation. The ubiquitous C 1s peak (≈285 eV) likely originates from adventitious carbon contamination, a common artifact in air-exposed samples, while the dominant O 1s peak (≈530 eV) reflects the oxygen lattice in both BFO and CTO phases. The atomic percentages derived from XPS as shown in Figure 3b correlate with the nominal BFO-to-CTO ratios, revealing systematic trends: higher BFO content (e.g., 60BFO-40CTO) corresponds to increased Fe atomic percentages, while higher CTO proportions (e.g., 40BFO-60CTO) show elevated Ca and Ti levels. This stoichiometric alignment confirms successful compositional tuning of the composites. However, the oxygen content remains relatively stable across all samples, suggesting robust oxygen coordination in the perovskite framework despite varying Fe/Ca/Ti ratios. These findings underscore the interplay between composition and surface chemistry in BFO-CTO composites. The tunable elemental ratios and stable oxygen sublattice suggest tailored electronic properties, making these materials promising for advanced applications. The XPS spectra details for the thick films of these composites are given in Supporting Information along with Figure S4 and Table S5 (Supporting Information). The material atomic percentage from XPS results was calculated based on reported work.[22]

The narrow or high-resolution scan spectra of Ca, Bi, Ti, O, C, and Fe are shown in **Figure 4** for 60BFO-40CTO. The similar spectra for 40BFO-60CTO and 50BFO-50CTO are given in Figure S5 (Supporting Information). The deconvoluted Ca 2p XPS spectra are shown in Figure 4a and Figure S5a,g (Supporting Information). The Ca 2p high-resolution XPS spectra have two distinct peaks within the binding energy range from 340 to 357 eV. In Figure 4a, the peaks centered ≈347.8 and 351.7 eV correspond to the Ca $2p_{3/2}$ and Ca $2p_{1/2}$ levels, respectively.[23] The Ca 2p peaks are slightly shifted to higher binding energy than those shown in Figure S5a,g (Supporting Information), attributing to a change in the BFO to CTO composite ratio, as discussed in the Supporting Information. Figure 4b, and Figure S5b,h (Supporting Information) shows high-resolution spectra of Bi 4f deconvoluted with two intense peaks at ≈158.0 and ≈163.3 eV, attributed to Bi $4f_{7/2}$ and Bi $4f_{5/2}$ with spin-orbit splitting of 5.3 eV. This is in good agreement with the Bi 4f spectral reported in literature without any considerable shift in the binding energy value of the peaks, representing the presence of the Bi^{3+} state due to Bi_2O_3. Nevertheless, sample 60BFO-40CTO reveals four prominent peaks, as depicted in Figure 4b and deconvoluted. The peaks positioned at 157.8 and 163.3 eV are indicative of the presence of metallic bismuth satellites ($Bi^{(0)}$ $4f_{7/2}$ and $Bi^{(0)}$ $4f_{5/2}$) with energetic spin-orbit splitting of 5.4 eV. The peaks appear at 159.4 and 165.8 eV ascribed to the binding energies of Bi $4f_{7/2}$ and Bi $4f_{5/2}$ (Bi^{3+}) with spin-orbit splitting of 5.3 eV.[24] The binding energies of Bi $4f_{7/2}$ and Bi $4f_{5/2}$ peaks obtained from 60BFO-40CTO

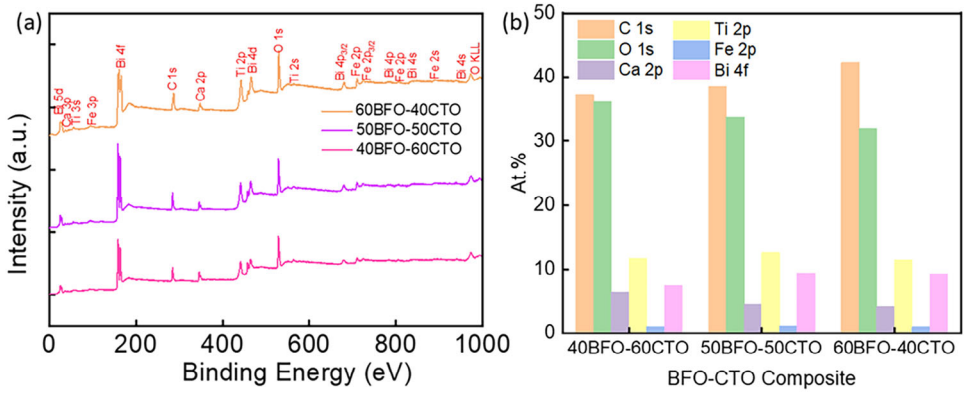

Figure 3. a) XPS survey spectral of BFO-CTO samples and b) Atomic percentages obtained from XPS measurements for BFO-CTO composite samples.

sample are slightly shifted to the higher energy than 40BFO-60CTO and 50BFO-50CTO samples. The presence of both metallic bismuth ($Bi^{(0)}$) and Bi_2O_3 (Bi^{3+}) can be explained by the possibility that as the BFO to CTO content ratio increases, the Bi^{3+} ions may be gaining electrons to transition into metallic bismuth ($Bi^{(0)}$).

Similarly, Figure 4c and Figure S5c,i (Supporting Information) shows narrow-band deconvoluted Ti 2p XPS spectra, in which two distinct peaks are observed. The peaks that occurred at 457.5 and 464.6 eV are ascribed to the Ti $2p_{3/2}$ and Ti $2p_{1/2}$ levels of Ti^{3+}.[25] This suggests that titanium sesquioxide (Ti_2O_3) dominates in the BFO-CTO nanocomposite samples. The O 1s XPS spectra exhibit a prominent peak at 528.5 eV and a shoulder peak at 529.8 eV, depicted in Figure 4d and Figure S5d,j (Supporting Information). This 528.5 and 529.8 eV peaks are attributed to oxygen within the oxide lattice and surface hydroxyl (OH) groups, respectively.[26] In this study, the C 1s peak was utilized for binding energy calibration, with the peaks at 284.1, 285.3, and 287.8 eV corresponding to C—C bonds, C—O bonds, and O—C=O bonds, as illustrated in Figure 4e and Figure S5e,k (Supporting Information).[27] Figure 4f and Figure S5f,l (Supporting Information) illustrate the high-resolution spectra from Fe 2p with doublet spin-orbit splitting Fe $2p_{1/2}$ and Fe $2p_{3/2}$. The binding energies from Fe^{3+} $2p_{3/2}$ and Fe^{2+} $2p_{3/2}$ have peaks

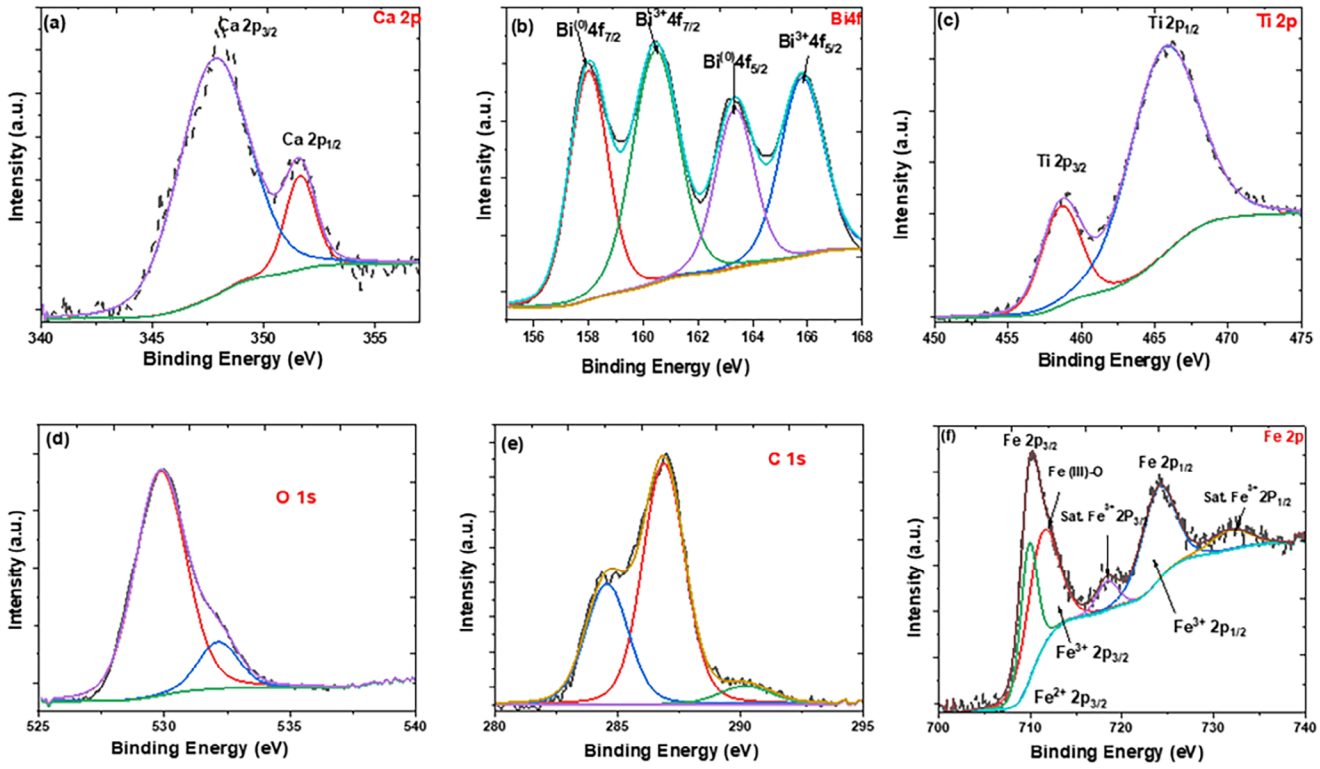

Figure 4. X-ray photoelectron (XPS) spectra of 60BFO-40CTO a) high-resolution scan of Ca 2p, b) high-resolution scan of Bi 4f, c) high-resolution scan of Ti 2p, d) high-resolution scan of O 1s, e) high-resolution scan of C1 1s, and f) high-resolution scan of Fe 2p.

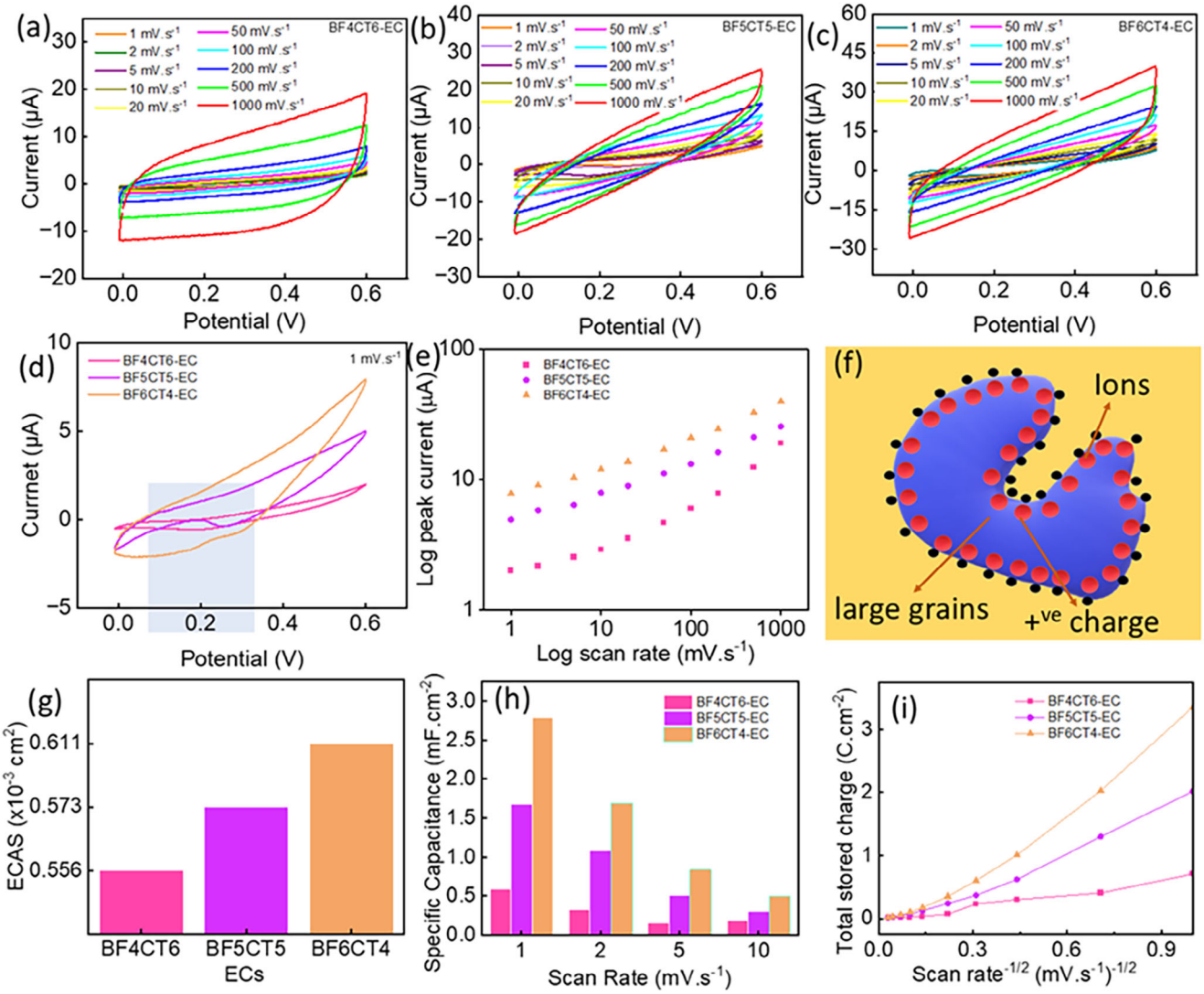

Figure 5. Electrochemical performances of the developed ECs. a) CV of BF4CT6 cell, b) CV of BF5CT5 cell, c) CV of BF6CT4 cell, d) Combined CV at 1 mV S^{-1}, e) log peak current versus log scan rate for all three devices f) schematic representation of the ion distribution around large grains in the electrode for 40BFO-60CTO.

centered at 709.8 and 711.3 eV, respectively.[28] The Fe 2p XPS spectra of BFO-CTO samples show distinct satellites at 718.4 and 732.1 eV, which are indicative of Fe^{3+} photoemission observed in Figure 4f and Figure S5l (Supporting Information).[29] The Fe^{2+} satellite was observed to have a binding energy of 712.8 eV from the 40BFO-60BFO (Figure S5f, Supporting Information) sample, which closely aligns with the reported value from magnetite.[30] The presence of both Fe^{2+} and Fe^{3+} species from the composite nanoparticles may be attributed to the existence of different oxides and hydroxides.

2.2. Electrochemical Characterization of Symmetrical EC

Cyclic voltammetry (CV) analysis was carried out for the symmetric devices BF4CT6-EC, BF5CT5-EC, and BF6CT4-EC to evaluate the best performance of the composite electrode. **Figure** 5a–c presents the CV curves for these devices across scan rates ranging from 1 to 1000 mV s^{-1}. In all devices, ions are reversibly stored in the electrode, as indicated by the nearly rectangular shapes of the CV curves and their mirror-image current responses upon voltage reversal. This behavior is particularly evident at high scan rates.[31] During the electrochemical reaction, small reduction peaks are visible for all three devices at low scan rates, such as one mV s^{-1} which is marked in Figure 5d. This is due to the intercalation and deintercalation of ions into the core of the electrode at a low scan rate. These peaks disappear at a high scan rate, and the CV curve shows more pseudo-rectangular shapes as given in Figure S6a,b (Supporting Information). Furthermore, we noticed that the changes in the ratio of BFO and CTO lead to variation in the peak current and area under the CV curve, as observed in Figure 5d,e. With the increase in the scan rate, the peak current for all devices was increased and is shown in Figure 5e. The electrode with 60BFO-40CTO shows a high peak

current due to more electrode-electrolyte interaction. The hydrophilic nature (Figure 2i–l) and the observed crystalline surface (Figure 2a–c) of this prepared electrode, there is an enhanced interaction between the electrolyte and electrode materials, which leads to enhanced ion interaction as schematically represented in Figure 5f for 40BFO-60CTO. A similar schematic representation for 60BFO-40CTO is given in Figure 1h, for 40BFO-60CTO in Figure 2f and for 50BFO-50CTO in Figure S7 (Supporting Information). In the 60BFO-40CTO electrode, we observed a structurally oriented large number of different sizes and shaped particles with multiple pores, as given in Figure 2g. During the electrochemical reaction, ions interact with all the particles, as shown in Figure 1h, leading to an enhanced ECSA for ion storage. The high conductivity (Figure 1g) and excellent wettability (Figure 2k) of the 60BFO-40CTO electrode further contribute to the increased ECSA. Additionally, a higher percentage of BFO improves ion intercalation and deintercalation into the electrodes, enhancing the electrode's stability and ability to handle higher currents.[32]

The influence of the electrode surface has a significant contribution to the energy-storing performances of the perovskite materials, as confirmed by the CV analysis. The ECSA of an electrode is calculated from the double-layer capacitance using the equation ECSA = C_{DL}/C_s, where C_s represents the sample's specific capacitance or the capacitance of an atomically smooth planar surface of the material per unit area under identical electrolyte conditions. Even though the smooth and planar surface of the electrode is significant for the measurement of C_s and ECSA, the printed film does not exhibit a smooth surface here. However, specific capacitances have been measured for a variety of metal electrodes in acidic and alkaline solutions, with typical values ranging from C_s = 0.015-0.110 mF cm^{-2} in H_2SO_4 to C_s = 0.022-0.130 mF cm^{-2} in NaOH and KOH.[33] Here, we consider the C_s value 0.022 mF.cm^{-2}. The double layer capacitance (C_{dl}) was determined by analyzing the slope of a linear regression between current density differences ($\Delta j/2 = (j_a\text{-}j_c)/2$) in the middle of the potential window of CV curves and scan rates, as given in Figure S8 (Supporting Information). The variation of measured ECSA of the three devices is shown in Figure 5g, which reveals a high value for 60BFO-40CTO-based electrodes. Due to these high performances, the BF6CT4-EC give a high specific capacitance of 2.79 mF.cm^{-2} (calculated using Equation S5, Supporting Information) compared to the other two devices, as shown in Figure 5h. The specific capacitance of all devices decreased with increasing scan rate, as shown in Figure 5h. The energy density of these devices was measured using the expression in Equation S2 (Supporting Information) and plotted in Figure S9 (Supporting Information). Here, the BF6CT4-EC shows a high energy density of 0.14 mWh cm^{-2} compared with BF5CT5-EC (0.08 mWh.cm^{-2}) and BF4CT6-EC (0.03 mWh.cm^{-2}). The diffusion of ions leads to a high charge storage contribution in BF6CT4-EC compared to the two other devices, as shown in Figure 5i, which is measured using the expression Equation S9 (Supporting Information).

The electrochemical impedance spectroscopy (EIS) data expressed through the Nyquist plots of the three cells are depicted in **Figure 6a**, and their behavior in different frequency ranges is marked in Figure S10 (Supporting Information). The lower frequencies region signifies resistive low equivalent series resistance (R_s) and fast interfacial processes, indicating optimal capacitance behavior for BFO-CTO cells. The lower frequency region of the Nyquist plot displays a characteristic straight line with a slope, which indicates diffusion-controlled Warburg impedance, which is represented by a 45° line, is related to the movement of ions between the electrolyte and electrode. This happens when there's a delay in ion movement, and the current is controlled by the diffusion of ions in the electrolyte toward the electrode.[34] The EIS data from Figure 6a shows that in low frequency, the magnitude of impedance, both real and imaginary, gives a lower value for BF6CT4-EC (given in Figure S11a,b, Supporting Information), which indicates faster ion diffusion in the electrode. These plots reveal a large incomplete semi-circle in medium frequencies for BF4CT6-EC and a small incomplete semi-circle for the other two devices, indicating Charge transfer resistance (R_{ct}) in the electrode materials. Due to the high resistance (as shown in Figure 1g) and low ECSA of the BF4CT6- EC electrode (Figure 5g), it exhibits a high charge transfer resistance (R_{ct}) value. Hence, as shown in Figure 6a, BF4CT6-EC exhibits the highest R_{ct}, while BF6CT4-EC demonstrates the lowest. Here, we observed that increasing the presence of $BiFeO_3$ facilitates more ion transfer from its crystal lattice, contributing to BF6CT4-EC having the least charge transfer resistance. In higher frequency regions, the value of R_s becomes significant, as marked in Figure S10 (Supporting Information). The zoomed image reveals a slight variation in contact resistance, which is small and consistent among the three cells, indicating good conductivity and excellent cell assembly. The R_s encompasses electrolyte ionic resistance, active material intrinsic resistance, and contact resistance at the active material-current collector interface.

The capacitive behavior of the three cells is further confirmed through Bode phase angle and impedance plot analysis and is presented in Figure S12a,b (Supporting Information). The Bode impedance decreases with increasing frequency, representing the capacitive nature of the electrode. We noticed that the phase angle reached a maximum value of −63° for BF6CT4-EC at 10 mHz, which closely resembles the ideal capacitor's phase angle of −90°. The real (C′) and imaginary (C″) capacitance components are estimated and shown in Figure S12c,d (Supporting Information) based on the EIS spectra. From these graphs, we observed BF6CT4-EC exhibit high C′ and C″, which is 0.5 mF.cm^{-2} and 1 $mFcm^{-2}$ at 10 mHz and is measured using Equations S6 and S7 (Supporting Information). The magnitude of the capacitance is shown in Figure S12e (Supporting Information) and is measured by Equation S8 (Supporting Information). The merit of all three devices was defined by the relaxation time constant (τ_0), which distinguishes between resistive and capacitive behaviors. A low τ_0 value indicates a high-power posture, which supports the capacitive property.[35] The value of τ_0 is typically calculated using $\tau_0 = 1/f_o$ with a projected phase angle of 45^0 as capacitive and resistive impedances are identical here. The time constant calculated from the Bode plot of 3 cells gives 207.24 ms for BF4CT6-EC, 138.16 ms for BF5CT5-EC and 37.68 ms for BF6CT4-EC and is presented in Figure S12f (Supporting Information). The low relaxation time represents the fast charging and discharging of the device, and hence, it gives BF6CT4-EC.

The electrochemical properties of the as-prepared electrodes were investigated further by conducting galvanostatic charge-discharge (GCD) measurements at various current densities 20, 30, 40, and 50 μA.cm^{-2} of all the fabricated 3 cells in Figure 6b (BF6CT4-EC), Figure S13a (Supporting Information)

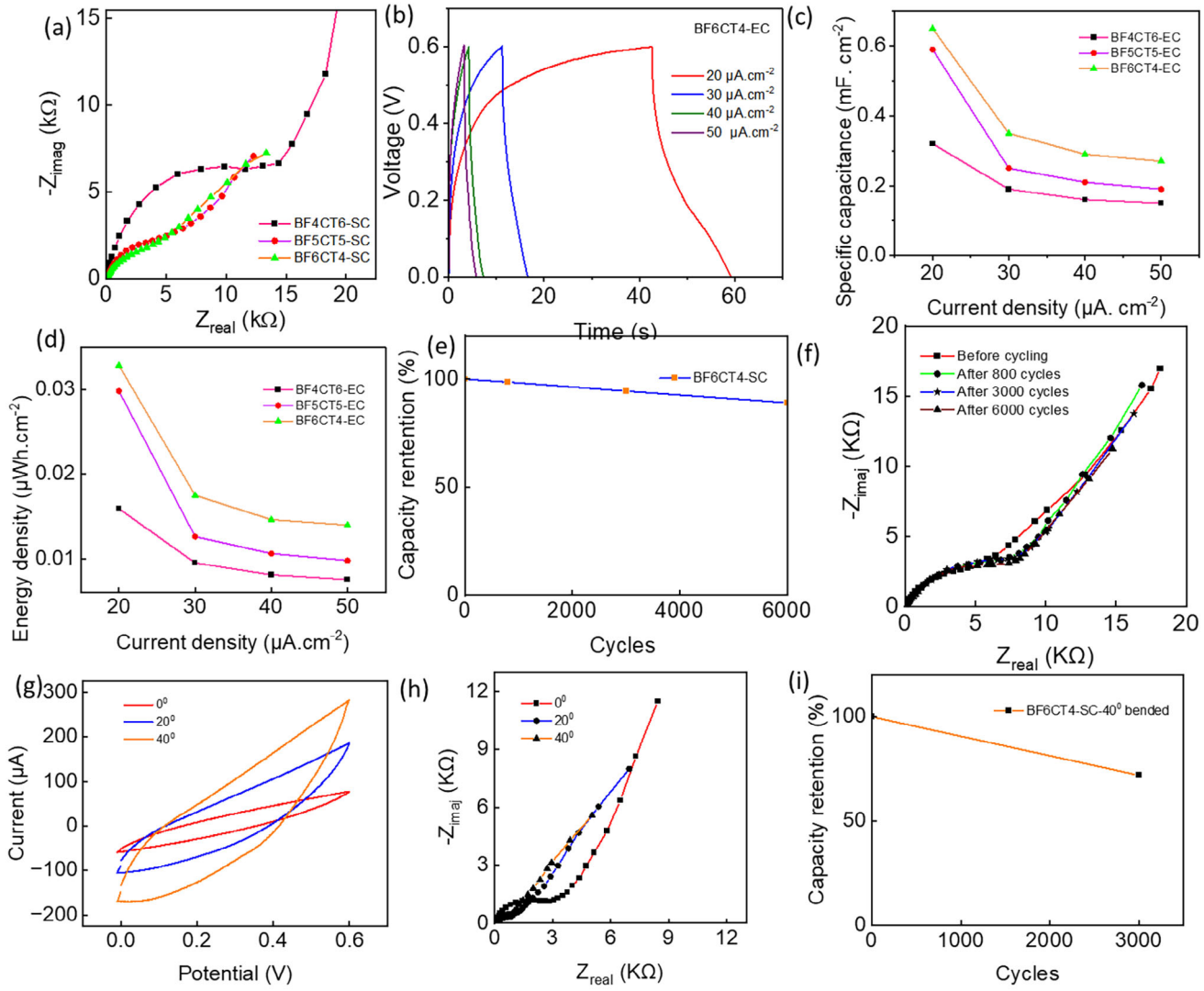

Figure 6. a) Nyquist plots of all the symmetric devices, b) GCD of BF6CT4 -EC, c) Specific capacitance of all the symmetric devices d) Energy density of all the symmetric devices. e) Capacity retention of BF6CT4-EC, f) Impedance growth of BF6CT4-EC while cycling, g) CV of BF6CT4-EC under various bending, h) Impedance variation of BF6CT4-EC under various bending and i) Capacity retention of BF4CT6-EC under 40^0 bending.

(BF4CT6-EC) and S13b (Supporting Information) (BF5CT5-EC). The GCD curves can be used to determine the reversibility of electrode materials during the charging/discharging process. Due to pseudocapacitive (PC) behavior, the GCD curve distorted from a symmetric triangle in the lowest current density of 20 $\mu A.cm^{-2}$ and is observed for all three ECs. In lower current density, the ions take more time to penetrate the inner bulk of the electrode material. Same as observed in the CV analysis. In lower current density, electric double-layer capacitance (EDLC) and PC behavior are visible, which leads to more specific capacitance. The BF6CT4-EC is showing better specific capacitance in 20 $\mu A.cm^{-2}$ ≈0.65 $mF.cm^{-2}$ and BF4CT6-EC and BF5CT5-EC are 0.32 $mF.cm^{-2}$ and 0.59 $mF.cm^{-2}$ respectively. In Figure 6c, it is visible that specific capacitance decreases with the increase in current density. The energy density of the 3 devices is shown in Figure 6d, which is proportional to the specific capacitance of the cells. The BF6CT4-EC is showing better energy density in 20 $\mu A.cm^{-2}$ ≈0.0325μWh. cm^{-2} and BF4CT6-EC and BF5CT5-EC are 0.016 $\mu Wh.cm^{-2}$ and 0.0295 $\mu Wh.cm^{-2}$ respectively. All ECs exhibit almost insignificant IR_{drops} at various current densities, indicating a low internal resistance. This helps in the fast movement of ions and leads to good power density.[36] The power density of developed ECs is shown in Figure S14 (Supporting Information) and calculated using the expression Equation S3 (Supporting Information).

Cyclic stability is one of the most critical parameters that reflect energy storage performance and define the efficiency of EC, which can be expressed in terms of specific capacitance and capacitance retention (%). The cyclic stability of the BFO-CTO electrode in the KOH electrolyte was investigated by repeating GCD measurements over 6000 cycles with a voltage window of 0 to 0.6 V at a current density of 50 $\mu A.cm^{-2}$ is shown in Figure 6e. The BF6CT4-EC is showing 90% capacity retention after 6000 cycles. The growth of EIS is carried out at different points between

6000 cycles, as shown in Figure 6f. The R_{ct} is increased to 1.6 times at 6000 cycles. This increase in the impedance resulted in the reduction of the capacitance.

The device is subjected to bending degrees of 20° and 40° to evaluate the flexibility of the EC. Figure S15a (Supporting Information) shows the flexibility of BF6CT4-EC under varying degrees of bending. CV, EIS, and GCD are carried out at different bending angles. From the CV curve, capacitance increases in bending angles, as shown in Figure 6g. The specific capacitance is increased by 3.4 times at 40° bending, this increase is due to the increase in the contact between the two electrodes. This is also verified in GCD shown in Figure S15b (Supporting Information), the increase in the specific capacitance is also due to the reduction of the resistance and it is shown in EIS analysis in Figure 6h. When the bendability increases, the contact between two electrodes improves and results in a decrease in the overall resistance of the device. Furthermore, the device evaluated the cycle stability at 40° bending at 200 $\mu A.cm^{-1}$ and is observed from GCD analysis (the first and last cycles are shown in Figure S15c (Supporting Information). The BF6CT4-EC shows 72% capacity retention after 3000 cycles, as shown in Figure 6i. The EIS growth occurs at various points between 3000 cycles, as illustrated in Figure S15d (Supporting Information). Over time, the device's resistance increased, resulting in a decrease in capacitance. The failure mechanisms typically involve both the destruction of electrode materials and interface issues.[37] One common failure pathway is the physical destruction of electrode materials. Under bending, electrodes can develop cracks or even tears at the place of highest stress. In some cases, the active material of the electrode can become detached due to mechanical fatigue, which not only reduces the effective surface area for electrochemical reactions but can also lead to short circuits if the loose particles bridge the gap between electrodes. Interface issues are another significant source of failure during static bending. The interfaces between different layers, such as between the electrode and the current collector, or between the electrode and the separator, can suffer from adhesion loss due to repeated mechanical stress, which creates high resistance.[37] The bending analysis shows that these ECs could be integrated into flexible circuits to run low-powered sensors and electronic components for wearables and smart devices.

We have carried out the post-mortem characterization of BF6CT4-EC. The SEM Figure S16a,b (Supporting Information) shows the structural variation of the electrode before and after 6000 cycles. Initially, the electrode surface exhibits a granular structure with well-defined and uniformly distributed particles with porous structures. After 6000 cycles, the electrode surface becomes rough and uneven. The particles clump together, and the porous structure gets reduced. This happens because the repeated cycles cause stress, breaking down the material and making it less stable.

Also, we carried out pre- and post-FTIR of the BF6CT4-EC electrode. An Ex-suit FTIR spectrum was measured using the 60BFO-40CTO electrode, both before and after cycling, to analyze chemical changes on the electrode surface. [1]The sample was measured in the wavenumber range from 400 to 4000 cm^{-1}. Figure S17 (Supporting Information) compares the FTIR spectra of the electrode before and after cycling, highlighting significant peaks as shown in Table S6. The peak details are provided in the supporting information. The elemental mapping was also carried out for the device before and after cycling, and the observed mapping is shown in Figure S18 (Supporting Information). The repeatability in performances of three devices evaluated, and it shows negligible variations as shown in Figure S19 (Supporting Information).

Further to this, we also measured the leakage current for the symmetric EC by connecting to a digital multimeter. BFO is known to behave as a conductive ceramic due to valence fluctuations of "Fe-ions", i.e., the Fe^{3+} to Fe^{2+} transition, in which oxygen vacancies act as charge carriers, thereby increasing leakage current. As a result, the reduced leakage current could be attributed to the suppression of the valence fluctuation of "Fe" ions in current BFO-CTO ceramics. The transition of Fe^{3+} to Fe^{2+} has been reported in BFO-based ceramics for partial substitution with analogous ions (Ti, Mn, Al, and Co) type solid solution compositions. In the presence of CTO, partial substitution of Ti^{4+} ions at BFO's 'Fe' sites is anticipated to suppress Fe valence fluctuations, lowering leakage current.[38] The BFO has a leakage current of 10^{-4} $A.cm^{-2}$, which is improved to $\approx 10^{-7}$ $A.cm^{-2}$ by doping with manganese.[39] BFO doped with zinc showed a leakage current of 0.562 mA.[40] The BF6CT4-EC was charged to the rated voltage using constant current mode and maintained at the rated voltage using constant voltage mode for 72 h. The device exhibited a reduced leakage current of 3 $\mu A.cm^{-2}$.

2.3. Electrochemical Characterization of Asymmetrical EC

The electrochemical investigation shows that among the three symmetrical ECs, the BF6CT4-based electrode exhibited excellent performance. Based on this, we further developed asymmetric EC with 60BF0-40CT0 on one electrode and another electrode with printed graphite, as shown in Figure 1e, which is named BF6CT4-G-EC. The CV is evaluated from a scan rate of 1 to 1000 $mV.s^{-1,}$ as shown in **Figure 7a**. The CV analysis shows that, as compared to symmetric EC, the asymmetrical devices show a large CV curve area, as shown in Figure S20a (Supporting Information) for 1 $mV.s^{-1}$. The specific capacitance measurement shows that the asymmetric cell has high performance and is 3.5 $mF.cm^{-2}$ at 1 $mV.s^{-1}$ and is higher than for BF6CT4-EC, which is 2.79 $mF.cm^{-2}$. The variation of specific capacitance with scan rate for both devices is compared in Figure 7b. This enhancement in the specific capacitance also leads to an increase in the energy density of the device and is found to be 0.174 $\mu Wh.cm^{-2}$ for BF6CT4-G-EC and 0.14 $\mu Wh.cm^{-2}$ for BF6CT4-EC, as shown in Figure 7c. In addition to this, we also noticed that the changing electrode configuration leads to enhancement of the ECSA, and for the BF6CT4-G-EC, its value is 1.059×10^{-3} cm^2, which is 1.73 times higher than for BF6CT4-EC. Moreover, we also measured the charge contribution for this asymmetric device, which was higher than that of the symmetric device, shown in Figure 1i.

Further, the EIS of the BF6CT4-G-EC were carried out, and the Nyquist plot is shown in Figure 7d. The Nyquist plot shows that the impedance magnitude is higher for the asymmetric device than the symmetric device, and for both devices, diffusive Warburg impedance is observed. The Nyquist plot shows that the charge transfer and solution resistance are less for BF6CT4-G-EC than for BF6CT4-EC, which results in more specific capacitance

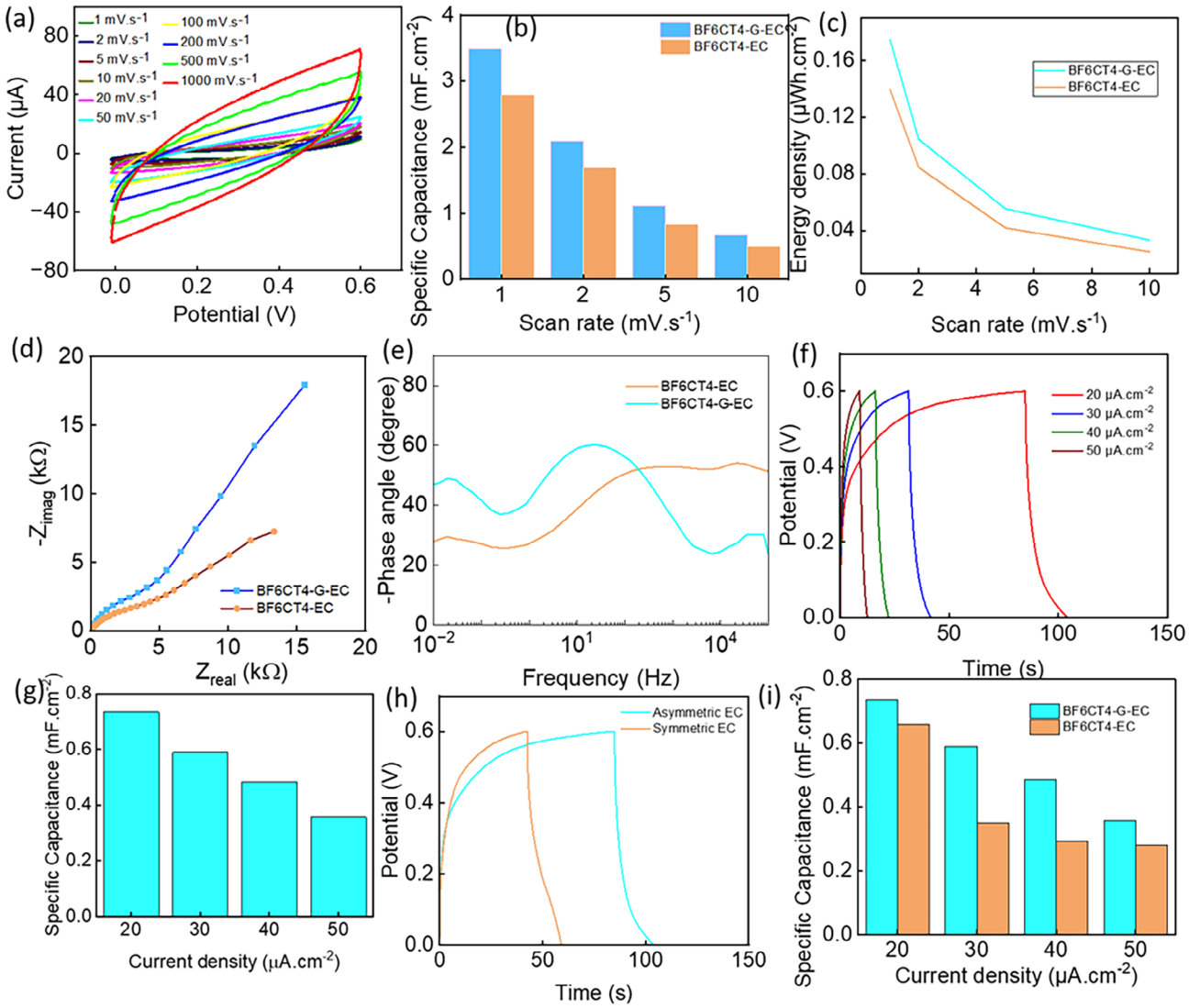

Figure 7. a) CV of BF6CT4-G-EC cell, b) Specific capacitance from CV of BF6CT4-EC and BF6CT4-G-EC's, c) Energy density of BF6CT4-EC and BF6CT4-G-EC's, d) Nyquist plot of BF6CT4-EC and BF6CT4-G-EC's, e) Phase angle of BF6CT4-EC and BF6CT4-G-EC's, f) GCD of BF6CT4-G-EC's, g) Specific capacitance from GCD of BF6CT4-G-EC's, h) GCD at 20 µA.cm^{-2} of BF6CT4-G-EC and BF6CT4-EC and i) Specific capacitance from GCD of BF6CT4-EC and BF6CT4-G-EC's.

and faster charging and discharging. The Bode impedance and phase angle plot for these two devices are shown in Figure S20b (Supporting Information) and Figure 7e, and they show similar behavior. The GCD analysis of the asymmetric device BF6CT4-G-EC is shown in Figure 7f and shows better specific capacitance than the symmetric BF6CT4-EC shown in Figure 7g. From this capacitance, the energy and power density were measured for various current densities of the asymmetric device and are shown in Figure S20c,d (Supporting Information). The asymmetric device exhibits energy density and power density of 0.036 µWh.cm^{-2} at 20 µA.cm^{-2} and 0.12 mW.cm^{-2} at 50 µA.cm^{-2}. The combined GCD at 20 µA.cm^{-2} of BF6CT4-G-EC and BF6CT4-EC is shown in Figure 7h, which has a specific capacitance of 0.73 and 0.65 mF.cm^{-2} respectively. The capacitance value of each current density of symmetric and asymmetric devices is in Figure 7i.

3. Conclusion

Here, we have demonstrated the application of perovskite material (1-x) $BiFeO_3$- $xCaTiO_3$ (x = 0.4,0.5,0.6) (BFO-CTO) as an electrochemical capacitor. We synthesized the BFO-CTO in 3 different ratios of 40-60, 50-50, and 60-40 through solid-state reaction and the prepared composite was printed on a flexible graphene sheet for the development of EC. From the crystalline properties through the XRD analysis, we noticed that a BFO and CTO was successfully formed in these compositions. Further, the morphological analysis, such as SEM images, predicts that the 60BFO-40CTO composite has multiple small-sized grains compared to another composite's big grains. The multiple different-sized grain particles are easily involved in electrochemical reactions and lead to an enhanced ECSA of 0.611 × 10^{-3} cm^2. Among the 3 ECs, it was observed that 60BFO-40CTO have better

electrochemical properties due to its high conductivity, wettability and crystalline properties and the high ECSA value. Further XPS analysis confirmed the mixture of metallic bismuth and bismuth oxide composite, which strongly contributed to the storage of BFO-CTO energy. The symmetric BF6CT4-EC exhibited a specific capacitance of 2.79 mF.cm^{-2} at 1 mV. S^{-1} has a good cycle stability of 90% after 6000 cycles. Also, it performed well under 20 and 40degree static bending and showed 72% capacity retention after 3000 cycles under bending 40 degrees. Compared with the symmetric EC, the asymmetric device with electrode configuration of 60BFO-40CTO versus graphite has a specific capacitance of 3.5 mF cm^{-2} at 1 mV^{-1}. Further, the GCD analysis of the asymmetric EC exhibits energy density and power density of 0.036 µWh.cm^{-2} at 20 µA.cm^{-2} and 0.12 mW.cm^{-2} at 50 µA.cm^{-2}. These values show the potential implementation of the BFO-CTO perovskite for low or ultra-low-powered (nW-µW) flexible and portable electronics applications.

4. Experimental Section

Preparation of Active Material: The active material (1-x) $BiFeO_3$-x$CaTiO_3$ (x = 0.4, 0.5, 0.6), abbreviated as (1-x)BFO-xCTO, based ceramic systems were synthesized using analytical-grade raw chemicals of Bi_2O_3, Fe_2O_3, $CaCO_3$, and TiO_2 through a conventional solid-state reaction method. Stoichiometric amounts of the dry raw powders were weighed and ball-milled for 6 h at a rotation speed of 300 rpm with a ball-to-powder weight ratio of 10:1 with Y_2O_3-stabilized ZrO_2 grinding media in isopropanol. The mixed powders were then calcined at 800 °C for 2 h and subsequently ball-milled again for 6 h before sintering. The dry powders were uniaxially pressed into pellets with a diameter of 8 mm and then sintered at 1150–1250 °C for 3 h in the air. After sintering, the pellets were crushed into powders using a mortar and pestle. XRD analysis of the powders was performed using a Bruker D8 ADVANCE with CuKα radiation (λ = 1.5406 Å).

In the present study, BFO - CTO with three ratios of 40-60%, 50-50%, and 60-40% and graphite (Merk) was used as the active materials for symmetric and unsymmetrical cells. Each active materials (80%) are mixed with a binder, ethyl cellouse (10%) (Sigma aldrich) and a conductive filler, carbon black (10%) (Alfa Aesar), in a solvent, terpinol (Sigma aldrich), with 25% loading separately. The slurry was coated on a graphene sheet current collector (Graphene supermarket) with an area of 1 cm^2 and a wire attached to it for making a connection outside. Before coating the active materials, the graphene sheet was attached to a flexible plastic sheet by using insulating paste and heated at 80 °C for 30 min. For strong adhesion of active materials on the graphene sheet after coating the materials heat heat-treated in an oven at 80 °C for 30 min. In the fabrication process, several strategies were implemented to maximize adhesion between active materials, current collectors, and flexible substrates. The slurries used for the electrode were optimized in terms of viscosity, solvent selection, and binder concentration to ensure uniform coverage and strong mechanical adhesion upon drying. The two identical active materials coated electrodes were sandwiched with a separator and aqueous electrolyte. Cellulose cloth was used as a separator. 6 M KOH (Sigma Aldrich) in DI water was used as an electrolyte. It has high ionic conductivity, allowing ions to move more freely, which facilitates faster charge and discharge cycles. The high concentration of free-moving K^+ and OH^- ions facilitates efficient charge transfer in the bulk electrolyte and at the electrode-electrolyte interface. The ability of EC to achieve fast charge and discharge rates depends on their high ionic conductivity, which qualifies them for high-power output applications. The high ionic conductivity results in lower internal resistance, which reduces energy losses due to heat generation and enables efficient energy storage. It was a sensible option for many applications because it raises fewer safety and environmental issues. BF4CT6, BF5CT5, and BF6CT4 are cells fabricated using three different composite active materials (Table S3, Supporting Information). The device fabrication schematic is provided in the Figure S1 (Supporting Information).

Material and Electrode Characterization: Scanning electron microscopy (SEM), mainly used for particle morphology screening, was carried out with a TESCAN-VEGA 3 scanning electron microscope at a working distance of 15 mm and an accelerating voltage of 20 kV. For the BFO-CTO electrodes, the SEM was taken at 2000 times and 4000 times magnification. For the graphite electrode, images were taken at 6000 magnification. SEM of before and after cycling electrode took with Hitachi S-4800 Cold Field Emission High-Resolution Scanning Electron Microscope. The energy-dispersive X-ray (EDX) of the electrode sample was also carried out using the same experimental setup. Fourier Transform Infrared Spectroscopy (FTIR) was conducted using a Perkin Elmer Frontier FTIR machine. The Raman spectroscopy of the BFO-CTO electrode was measured using the Renishaw inVia Raman Microscope, which has a 488 nm diode excitation source and a power of 25 mW. The sample was positioned on the mounting stage, and spectral data was collected using a 50X objective. An XPS analysis was performed with the Thermo Scientific K-alpha X-ray Photoelectron Spectrometer (Thermo Scientific, East Grinstead, UK) and survey spectra with a broad energy range and multiple elements were obtained. BFO-CTO powdered and electrode were cast into Al discs and held in place on SEM stubs with double-sided carbon tape. The surface sample underwent decontamination by exposure to clusters of Ar gas containing ≈1000 atoms per cluster at an energy level of 4 keV for 60 s. The scans were conducted between -5.0 and 1350.0 eV, with a dwell time of 50 ms, a step size of 1.0 eV, and a pass energy of 200.0 eV. High-resolution carbon 1s (C1s) and BFO-CTO powdered samples were obtained utilizing a 40 eV pass energy and a 0.1 eV step size. The narrow band spectra of each element were attained using a monochromatic Al Kα X-ray source with an output energy of 1486.6 eV and a maximum X-ray beam spot size of 400 µm. The spectral analysis was performed using CasaXPS software (CasaXPS Ltd, Teignmouth, UK). Major element peaks were identified and analyzed based on the Handbook of X-ray photoelectron spectroscopy. The Shirley-type background was employed to analyze all the high-resolution spectra and then fitted with Gaussian components.

Furthermore, the contact angle was measured with Ossila (Goniometer L2004A1) equipment. One drop of electrolyte was added to the top of the electrode separately, and the image was captured by its software (Ossila Contact Angle v3.1.2.2). The picture was captured at 10 s and 10 min after the electrolyte dropped. The sheet resistance of the electrode is measured by Ossila (T2001A4) four-probe measurement. The measurement was taken at different areas of the electrode by using the Ossila software (Ocilla Sheet Resistance Lite v1.0.4.1). The VESTA tool was used to visualize the crystalline structure of CTO and BFO materials.

Electrochemical Characterization: To explore the application of the $BiFeO_3$ - $CaTiO_3$ electrode as a promising EC, the electrochemical characterizations were performed with cyclic voltammetry (CV), Galvanostatic charge-discharge (GCD), and electrochemical impedance spectroscopy (EIS) measurements. The CV was taken at different scan rates, from 1 mV.s^{-1} to 1000 mV.s^{-1}. GCD is taken at different current rates, and EIS was recorded from 10 mHz to 100 kHz. These electrochemical characterizations were carried out by Ivium equipment. The operating potential was taken as 0 to 0.6 V. To determine the electrochemical performance of the electrode as an EC, the data were analyzed from the electrochemical characterization technique by using the equations given in the Supporting Information. To evaluate the device's performance in gel electrolyte, experiments were also carried out in BF6CT4 with PVA-LiCl and the details are provided in the Supporting Information with device properties (Figure S21, Supporting Information). The static bending was carried out by the device mounted on the surface of 2 bottles with diameters of 1.6 and 2.7 cm, with 40 and 20 degrees, respectively. Adhesion of the active electrode on the current collector was evaluated through bending testing and electrochemical cycling under deformation. The devices show stable performance over repeated bending conditions, indicating reliable interface integrity. The leakage current measurement of the device was carried out by charging to the rated voltage (0.6 V) using constant current mode and maintaining at the rated voltage using constant voltage mode

for 72 h. The current showing after 72 h was the leakage current of the device.

Supporting Information

Supporting Information is available from the Wiley Online Library or from the author.

Acknowledgements

This work was supported by the Edinburgh Napier University SCEBE Starter Grant (N480-001) and L.M. acknowledged The Carnegie Trust for the Universities of Scotland Grant (R2552-00). G.J. acknowledged EPSRC grant (EP/T004711/1). This work was supported by the Royal Society of Chemistry Research Fund Grant (R23-0577995877).

Conflict of Interest

The authors declare no conflict of interest.

Data Availability Statement

The data that support the findings of this study are available from the corresponding author upon reasonable request.

Keywords

energy storage, flexible electrochemical capacitors, perovskite material

Received: March 26, 2025
Revised: June 30, 2025
Published online:

[1] a) X. Tong, Z. Tian, J. Sun, V. Tung, R. B. Kaner, Y. Shao, *Mater. Today* **2021**, *44*, 78; b) J. Li, P. Yang, X. Li, C. Jiang, J. Yun, W. Yan, K. Liu, H. J. Fan, S. W. Lee, *ACS Energy Lett.* **2023**, *8*, 1; c) L. Manjakkal, A. Pullanchiyodan, N. Yogeswaran, E. S. Hosseini, R. Dahiya, *Adv. Mater.* **2020**, *32*, 1907254; d) L. Manjakkal, L. Yin, A. Nathan, J. Wang, R. Dahiya, *Adv. Mater.* **2021**, *33*, 2100899.

[2] R. Schmuch, R. Wagner, G. Hörpel, T. Placke, M. Winter, *Nat. Energy* **2018**, *3*, 267.

[3] a) P. Goel, S. Sundriyal, V. Shrivastav, S. Mishra, D. P. Dubal, K.-H. Kim, A. Deep, *Nano Energy* **2021**, *80*, 105552; b) M. Mohan, N. P. Shetti, T. M. Aminabhavi, *J. Power Sources* **2023**, *574*, 233166; c) L. Zhang, J. Miao, J. Li, Q. Li, *Adv. Funct. Mater.* **2020**, *30*, 2003653; d) Z. Jia, C. Cheng, X. Chen, L. Liu, R. Ding, J. Ye, J. Wang, L. Fu, Y. Cheng, Y. Wu, *Mater. Adv.* **2023**, *4*, 79.

[4] M. Anaya, G. Lozano, M. E. Calvo, H. Míguez, *Joule* **2017**, *1*, 769.

[5] H. S. Magar, A. M. Mansour, A. B. A. Hammad, *Sci. Rep.* **2024**, *14*, 1849.

[6] M. Ahangari, J. Mostafaei, A. Sayyah, E. Mahmoudi, E. Asghari, A. Coruh, N. Delibas, A. Niaei, *J. Energy Storage* **2023**, *63*, 107034.

[7] a) J. Liang, G. Zhu, Z. Lu, P. Zhao, C. Wang, Y. Ma, Z. Xu, Y. Wang, Y. Hu, L. Ma, *J. Mater. Chem. A* **2018**, *6*, 2047; b) S. Gomasu, S. Saha, S. Ghosh, R. Bhowmik, D. Das, *ACS Appl. Mater. Interfaces* **2024**, *16*, 3654; c) G. Sreenu, S. Saha, R. N. Bhowmik, J. P. Praveen, D. Das, *J. Mater. Sci.: Mater. Electron.* **2022**, *33*, 24959.

[8] Q. Yin, K. Qiu, W. Zhang, X. Chen, P. Zhang, Q. Tang, M. Chen, *Opt. Mater.* **2019**, *98*, 109446.

[9] a) M. M. Lencka, R. E. Riman, *Chem. Mater.* **1995**, *7*, 18; b) D. Klimm, M. Schmidt, N. Wolff, C. Guguschev, S. Ganschow, *J. Cryst. Growth* **2018**, *486*, 117; c) L. B. Barbosa, D. R. Ardila, J. P. Andreeta, *J. Cryst. Growth* **2001**, *231*, 488.

[10] a) D. Moitra, C. Anand, B. K. Ghosh, M. Chandel, N. N. Ghosh, *ACS Appl. Energy Mater.* **2018**, *1*, 464; b) N. Wang, X. Luo, L. Han, Z. Zhang, R. Zhang, H. Olin, Y. Yang, *Nano-Micro Lett.* **2020**, *12*, 81.

[11] S. Jo, S. Pak, Y.-W. Lee, S. Cha, J. Hong, J. I. Sohn, *Int. J. Energy Res.* **2023**, *2023*, 2496447.

[12] a) H. Zubairi, Z. Lu, Y. Zhu, I. M. Reaney, G. Wang, *Chem. Soc. Rev.* **2024**, *53*, 10761; b) Z. Lu, G. Wang, W. Bao, J. Li, L. Li, A. Mostaed, H. Yang, H. Ji, D. Li, A. Feteira, F. Xu, D. C. Sinclair, D. Wang, S.-Y. Liu, I. M. Reaney, *Energy Environ. Sci.* **2020**, *13*, 2938; c) G. Wang, Z. Lu, Y. Li, L. Li, H. Ji, A. Feteira, D. Zhou, D. Wang, S. Zhang, I. M. Reaney, *Chem. Rev.* **2021**, *121*, 6124.

[13] R. Zohourian, R. Merkle, G. Raimondi, J. Maier, *Adv. Funct. Mater.* **2018**, *28*, 1801241.

[14] T. Ofoegbuna, P. Darapaneni, S. Sahu, C. Plaisance, J. A. Dorman, *Nanoscale* **2019**, *11*, 14303.

[15] J. S. Zhou, J. B. Goodenough, B. Dabrowski, P. W. Klamut, Z. Bukowski, *Phys. Rev. Lett.* **2000**, *84*, 526.

[16] D. N. Mueller, R. A. De Souza, J. Brendt, D. Samuelis, M. Martin, *J. Mater. Chem.* **2009**, *19*, 1960.

[17] I. O. Troyanchuk, D. V. Karpinsky, M. V. Bushinskii, O. Prokhnenko, M. Kopcevicz, R. Szymczak, J. Pietosa, *J. Exp. Theor. Phys.* **2008**, *107*, 83.

[18] C. M. Culbertson, A. T. Flak, M. Yatskin, P. H. Y. Cheong, D. P. Cann, M. R. Dolgos, *Sci. Rep.* **2020**, *10*, 3729.

[19] a) J. A. Sánchez-Márquez, R. Fuentes-Ramírez, I. Cano-Rodríguez, Z. Gamiño-Arroyo, E. Rubio-Rosas, J. M. Kenny, N. Rescignano, *Int. J. Polym. Sci.* **2015**, *2015*, 320631; b) S. Piqueras, S. Füchtner, R. Rocha de Oliveira, A. Gómez-Sánchez, S. Jelavić, T. Keplinger, A. de Juan, L. G. Thygesen, *Front. Plant Sci.* **2020**, *10*, 1701; c) S. P. Firsov, R. G. Zhbankov, *J. Appl. Spectrosc.* **1982**, *37*, 940.

[20] P. Tan, C. Hu, J. Dong, W. Shen, B. Zhang, *Phys. Rev. B* **2001**, *64*, 214301.

[21] a) M. Eledath, M. Chandran, *J. Phys. Chem. Solids* **2023**, *172*, 111060; b) H. Zheng, G. D. C. Csete de Györgyfalva, R. Quimby, H. Bagshaw, R. Ubic, I. M. Reaney, J. Yarwood, *J. Eur. Ceram. Soc.* **2003**, *23*, 2653.

[22] G. Zorn, S. R. Dave, X. Gao, D. G. Castner, *Anal. Chem.* **2011**, *83*, 866.

[23] Y. Yan, H. Yang, X. Zhao, H. Zhang, J. Jiang, *J. Electron. Mater.* **2018**, *47*, 3045.

[24] a) G. A. Gomez-Iriarte, A. Pentón-Madrigal, L. A. S. de Oliveira, J. P. Sinnecker, *Materials* **2022**, *15*, 4285; b) S. Chaturvedi, I. Sarkar, M. M. Shirolkar, U.-S. Jeng, Y.-Q. Yeh, R. Rajendra, N. Ballav, S. Kulkarni, *Appl. Phys. Lett.* **2014**, *105*, 102910.

[25] R. Sanjinés, H. Tang, H. Berger, F. Gozzo, G. Margaritondo, F. Lévy, *J. Appl. Phys.* **1994**, *75*, 2945.

[26] a) N. Shi, X. Li, T. Fan, H. Zhou, J. Ding, D. Zhang, H. Zhu, *Energy Environ. Sci.* **2011**, *4*, 172; b) D.-H. Wang, L. Jia, X.-L. Wu, L.-Q. Lu, A.-W. Xu, *Nanoscale* **2012**, *4*, 576.

[27] G. Greczynski, L. Hultman, *Sci. Rep.* **2021**, *11*, 11195.

[28] R. Balakrishnan, A. Dixit, M. S. R. Rao, R. Naik, *Surf. Interface Anal.* **2021**, *53*, 798.

[29] D. Giraldo, P. Almodóvar, M. L. López, E. Rodríguez-Aguado, E. Rodríguez-Castellón, A. Galdámez, I. Álvarez-Serrano, *J. Eur. Ceram. Soc.* **2021**, *41*, 7069.

[30] G. Bhargava, I. Gouzman, C. M. Chun, T. A. Ramanarayanan, S. L. Bernasek, *Appl. Surf. Sci.* **2007**, *253*, 4322.

[31] a) A. T. Mavelil, V. Sam, P. R. Markapudi, F. Paul, M. Beg, L. Manjakkal, *IEEE Sens. Lett.* **2024**, *8*, 1; b) M. Beg, K. M. Alcock, A. Titus Mavelil,

D. O'Rourke, D. Sun, K. Goh, L. Manjakkal, H. Yu, *ACS Appl. Mater. Interfaces* **2023**, *15*, 51100; c) F. Paul, V. K. Narayanan, S. S. Gopidas, P. R. Markapudi, C. H. See, G. Jose, S. N. Potty, L. Manjakkal, *Appl. Phys. Lett.* **2025**, *126*, 133901.

[32] Q. Pan, C. Yang, Q. Jia, W. Qi, H. Wei, M. Wang, S. Yang, B. Cao, *Chem. Eng. J.* **2020**, *397*, 125524.

[33] C. C. McCrory, S. Jung, J. C. Peters, T. F. Jaramillo, *J. Am. Chem. Soc.* **2013**, *135*, 16977.

[34] a) Q. Zhuang, *Acta Chim. Sin.* **2009**,*67*, 2184; b) Y. He, *AIP Adv.* **2022**, 12; c) W. Habib, A. Saji, F. Paul, P. R. Markapudi, C. Wilson, L. Manjakkal, *Results Eng.* **2025**, *25*, 104510.

[35] B. Pandit, S. S. Karade, B. R. Sankapal, *ACS Appl. Mater. Interfaces* **2017**, *9*, 44880.

[36] M. Prince, J. Kanathedath, F. Paul, P. R. Markapudi, M. Beg, L. Paterson, M. P. Desmulliez, S. C. Pillai, L. Manjakkal, *J. Power Sources* **2025**, *631*, 236214.

[37] a) Z. Fu, M. Hannula, A. Jauho, K.-L. Väisänen, M. Välimäki, J. Keskinen, M. Mäntysalo, *ACS Appl. Mater. Interfaces* **2022**, *14*, 40145; b) K. Kim, C. K. Chan, *Front. Batteries Electrochem.* **2024**, *3*, 1371167.

[38] a) R. K. Mansingh, R. K. Mishra, T. Dash, *AIP Conf. Proc.* **2021**, *2417*, 020021; b) H. Wu, J. Li, H. Bai, D. Zhao, Z. Zhou, *Mater. Lett.* **2024**, *354*, 135378.

[39] W. A. Wani, N. Naaz, B. H. Venkataraman, S. Kundu, K. Ramaswamy, *J. Phys.: Conf. Ser.* **2021**, *2070*, 012088.

[40] S. Yu, C. Yang, W. Wang, D. Han, W. Qi, R. Ling, S. Xu, G. Liu, *J. Ind. Eng. Chem.* **2024**, *138*, 415.